



Enhanced catalytic performance of graphene-TiO₂ nanocomposites for synergetic degradation of fluoroquinolone antibiotic in pulsed discharge plasma system

He Guo^a, Nan Jiang^{a,b,*}, Huijuan Wang^c, Kefeng Shang^{a,b}, Na Lu^{a,b}, Jie Li^{a,b}, Yan Wu^{a,b}

^a Key Laboratory of Industrial Ecology and Environmental Engineering (Ministry of Education, China), School of Environmental Science and Technology, Dalian University of Technology, Dalian 116024, China

^b School of Electrical Engineering, Dalian University of Technology, Dalian 116024, China

^c School of Environment and Safety Engineering, Jiangsu University, Zhenjiang 212013, China

ARTICLE INFO

Keywords:

Graphene-TiO₂
Photocatalysis
Flumequine
Degradation
Pulsed discharge plasma

ABSTRACT

A hybrid graphene-TiO₂ nanocomposites have been prepared by a facile hydrothermal method to improve the photocatalytic performance and applied for synergetic degradation of fluoroquinolone antibiotic in pulsed discharge plasma (PDP) system. The characterizations of the structure and morphology, chemical bonding state, optical property and electrochemical property show that the graphene-TiO₂ nanocomposites can be hybridized successfully. Compared to the pure TiO₂, the light absorption range can extend to visible light (< 505 nm) and the recombination rate of electron-hole pairs declines apparently in the graphene-TiO₂ samples. The degradation performance experiment manifests a significant enhancement of the removal efficiency of flumequine (FLU) when the graphene-TiO₂ samples are added in the PDP system. The highest removal efficiency can reach 99.4% in PDP/graphene-TiO₂ system with 5% graphene content, which is 23.7% and 34.6% higher than that in PDP/TiO₂ system and sole PDP system, respectively. Correspondingly, the kinetic constant is 3.5 and 4.6 times higher than that in PDP/TiO₂ system and sole PDP system, respectively. The radical species trapping test suggests that [•]OH, h⁺ and [•]O₂⁻ play the critical role for FLU degradation in PDP/graphene-TiO₂ system. The graphene-TiO₂ samples can further decompose the O₃ and improve the generation of [•]OH and H₂O₂. The degradation intermediates are determined by LC-MS and IC. The toxicity evolution of FLU reaction solutions is evaluated based on inhibition of photobacterium *V. fischeri*. Finally, the FLU degradation mechanism in the PDP/graphene-TiO₂ system is proposed. This research would provide a novel insight into the application of graphene-based nanocomposites in PDP system as a promising remediation methodology for organic contaminants in water.

1. Introduction

In recent decades, antibiotics have been used widely for controlling infectious disease of human, flora and fauna, and then ensured their body health [1]. Among antibiotics, fluoroquinolones (FQs) have been received considerable attention because of their broad antibacterial spectra with lower resistance during drug treatment of animal cultures [2,3]. However, due to abuse and inappropriate disposal, FQs have been found ubiquitously, such as sewage treatment plant, surface waters, ground water. Even at a very low concentration, FQs can cause inevitable harm to aquatic environment and human health [4]. Even more distressingly, since the extensive pollution, bioaccumulation and relatively stable physicochemical characteristics, conventional methods are difficult to eliminate them efficiently [5]. Consequently, dedicated

treating methods for the FQs wastewater have become urgently needed.

As one of advanced oxidation technologies (AOTs), non-thermal plasma (NTP) has been deemed as one of the most promising technologies for contaminant treatment in the past few years, including wastewater remediation, exhausted gas abatement and solid-waste disposal [6–8]. Especially for wastewater remediation, pulsed discharge plasma (PDP) has been received enthusiastic attention from international and domestic academics regarding to its easy operation, high efficiency and no second pollution. The generated high potential species, such as [•]OH, [•]O₂⁻, O₃ and H₂O₂ can react with organic pollutants fast and non-selectivity. Among those active species, [•]OH is considered to play a key role in degrading organic compounds. The technology has been successfully applied for the treatment of different wastewater, including dye [9], phenol [10], methane [11], p-chlorophenol [12] and humic

* Corresponding author at: School of Environmental Science and Technology, Dalian University of Technology, Dalian 116024, China.

E-mail address: jiangnan@dlut.edu.cn (N. Jiang).

<https://doi.org/10.1016/j.apcatb.2019.01.052>

Received 10 October 2018; Received in revised form 19 December 2018; Accepted 17 January 2019

Available online 25 January 2019

0926-3373/© 2019 Elsevier B.V. All rights reserved.

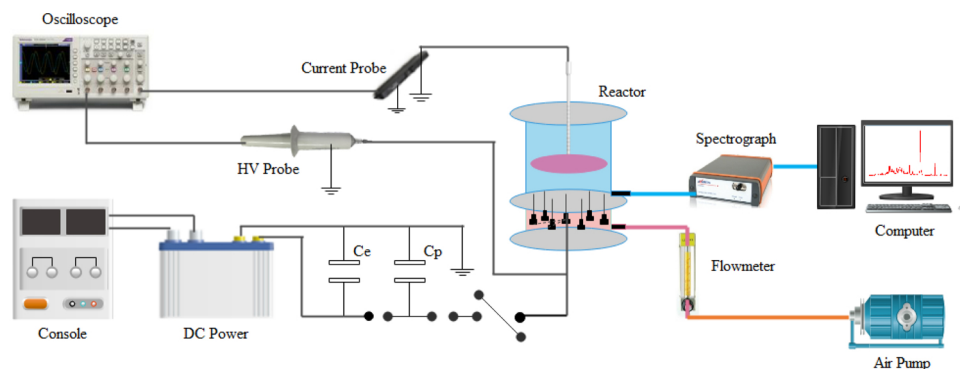


Fig. 1. Schematic diagram of the experimental system.

acid [13]. Notwithstanding, the lower energy efficiency has always restricted the development of the technology. Although many physical effects such as light, ultrasound and electricity can be generated during pulsed discharge, most of them are unable to fully utilize and release out the discharge area, which leads to the energy waste. In order to settle the issues, introduction of photocatalyst into PDP system becomes a major way with the purpose of the UV light exploitation. Many reports have addressed that PDP coupled with TiO_2 can make the best of UV light and enhance the removal of organic pollutants [14–19]. However, as is well-known, TiO_2 has a wide band gap of 3.2 eV, meaning that the required excitation wavelength is limited in the UV region ($< 380 \text{ nm}$). In fact, the UV light is relative weak compared to the visible light during the pulsed discharge in water [20,21]. That is to say, the visible light with higher intensity has not been exploited. Besides, the quick recombination of electron–hole pairs of TiO_2 has also reduced the photocatalytic efficiency. Therefore, further research focuses on exploiting the visible light generated from pulsed discharge and accelerating the separation of electron–hole pairs of TiO_2 .

It is worthy to note that graphene oxide (GO) is a novel carbon material, which has a two-dimensional honeycomb-like structure composed of sp^2 -hybridized carbon atoms. And it owns a lot of unique physical properties, such as high carrier mobility ($200,000 \text{ cm}^2 \text{ V}^{-1} \text{ S}^{-1}$), high specific surface area, favorable optical property and excellent electrical conductivity [22–25]. To date, researchers have employed the nano-semiconductor coupled with reduced graphene oxide (rGO) for improving property of single-phase photocatalyst. It has been reported that rGO based semiconductor composites could facilitate the effective photodegradation of pollutant during the photocatalysis because of the reduced band-gap and accelerative electron transparency [26–32]. In addition, the hybridization of photocatalyst and rGO can reduce the band gap of photocatalyst and make it active in visible light [33]. However, to the best of our knowledge, the application of rGO-based composites in PDP system for wastewater treatment has not been reported.

Based on this, we propose the application of rGO- TiO_2 nanocomposites in the PDP system for the purpose of wastewater treatment. Theoretically, the hybridization of TiO_2 and rGO can enhance the adsorption range of light, which exploits the visible light generated by PDP. Besides, TiO_2 hybrid with graphene can accelerate the separation of electron–hole pairs and improve its photocatalytic efficiency in the PDP system. Furthermore, the load of TiO_2 nanoparticles on graphene sheet can prevent them reunite and then enhance the contact area among TiO_2 , organic compounds and plasma.

Herein, this study is undertaken to prepare the hybrid rGO- TiO_2 nanocomposites, and combined with PDP for synergetic treatment of FQ wastewater. Flumequine (FLU), a representative FQ, is selected as the target compounds. The rGO- TiO_2 nanocomposites were prepared by hydrothermal method. The structure and morphology, chemical bonding state, optical property and electrochemical property and electronic structures of the prepared rGO- TiO_2 samples were

systematically characterized. The FLU degradation performance in PDP system with the obtained rGO- TiO_2 samples was evaluated. Then, the reuse property of the prepared sample in PDP system was monitored. Subsequently, the role of active species was evaluated, and the formation of active species was detected. TOC analyzer and three-dimensional excitation–emission matrix fluorescence spectroscopy (3D EEFMs) were used to further evaluate the mineralization ability of FLU degradation. The degradation intermediates were detected by LC–MS and IC, and a plausible degradation pathway for FLU was also proposed. The toxicity of FLU and the generated products was evaluated based on inhibition of bacterial luminescence. Based on the above research, the degradation mechanism of FLU was proposed eventually.

2. Experimental

2.1. Chemicals and reagents

TiO_2 (P25, 20% rutile and 80% anatase, $50 \text{ m}^2 \text{ g}^{-1}$, 21 nm) was purchased from Guangzhou HOCH trading Co., Ltd. FLU was purchased from Aladdin. Graphite, thick sulfuric acid, hydrochloric acid (HCl), sodium nitrate (NaNO_3), potassium permanganate (KMnO_4), hydrogen peroxide (H_2O_2), benzoquinone (BQ), sodium oxalate (SO), isopropyl alcohol (IPA), potassium iodide (KI) were purchased from Tianjin Kemiou Chemical Reagent Co., Ltd. All chemicals were used without further purification. The deionized water was used for all experiments.

2.2. Experimental setup

Fig. 1 represents the schematic diagram of experimental setup, which is made up of four major parts: pulsed power, reactor system, electrical detecting system and a spectrum detecting system. The detail information is provided in Supplementary Material.

2.3. Catalyst preparation

Details of the preparation of rGO- TiO_2 composites are provided in Supplementary Material. The prepared samples with different weight ratio of graphene to TiO_2 (1%–7%) are marked as rGTi-1, rGTi-2, rGTi-3, rGTi-4, rGTi-5, rGTi-6 and rGTi-7, respectively.

2.4. Characterizations

The crystal phases of the samples were evaluated by X-ray powder diffraction (XRD, Rigaku Corporation, D/MAX 2400) in the range of 5° – 90° (2θ), using Cu K α radiation. The morphologies of the obtained samples were characterized by scanning electron microscope (SEM, FEI, Nova Nano SEM 450) and transmission electron microscopy (TEM, Tecnai F30). X-ray photoelectron spectroscopy (XPS) was performed on a Thermo ESCALAB 250X. The UV–vis diffuse reflectance spectroscopy (DRS) was obtained via UV–vis spectrophotometer (Shimadzu, UV-550)

using BaSO₄ as a reference material. Fourier transform infrared (FT-IR) spectroscopy was performed on a Bruker MPA FTIR spectrometer. Raman spectra were detected on a microscopic confocal Raman spectrometer (Thermo Fisher, DXR Smart Raman). Photocurrents and electrochemical impedance spectroscopy (EIS) were determined by an electrochemical analyzer (CHI instruments 660E), using a standard three-electrode system. Photoluminescence (PL) spectra and 3D EEFMs were recorded on a fluorescence spectrophotometer (Hitachi, FL4500).

2.5. FLU degradation test

The detection of FLU concentration, and detail calculation process are shown in Supplementary Material. During the experiment, the peak voltage, frequency, electrode gap, air flow rate, FLU concentration, solution volume and catalyst weight were set as 18 kV, 50 Hz, 10 mm, 4 L/min, 40 mg/L, 0.15 L and 0.2 g/L, respectively. The concentration of O₃, ·OH and H₂O₂ were detected by a selective indigo method [34], trapping reagent salicylate [35] and titanium sulfate method [36] respectively. The mineralization was measured by TOC analyzer (Analytickjena, multi N/C 2100s). The degradation intermediates were identified by an ion chromatography (Thermo Scientific, DIONEX ICS-5000) and a liquid chromatography-tandem mass spectrometry (LC-MS/MS, Thermo Scientific, LTQ Orbitrap XL).

2.6. Toxicity assays

The toxicity of FLU and its generated products were evaluated based on inhibition of *Photobacterium V. fischeri* (NRRL B-11177). The detailed evaluated process is provided in Supplementary Material.

3. Results and discussion

3.1. Characterization of the graphene-TiO₂ samples

3.1.1. Structure and morphology

The crystal structures and phase purities of pure TiO₂ and rGO-TiO₂ samples are illustrated by XRD, which are presented in Fig. 2. It can be seen that pure TiO₂ exhibits both anatase crystal phase and rutile crystal phase, which is consistent with the commercial P25. The anatase crystal phase with the corresponding diffraction peak is well indexed to the (101), (004), (200), (105), (211), (204), (116), (220) and (215), and all values are in good agreement with JPCDS, No. 21-1272. The characteristic peaks of (110), (101) and (111) at 27.4°, 36.0° and 41.2° are ascribed to the rutile crystal phase (JPCDS, No. 21-1276). In the patterns of rGO-TiO₂ samples, there is no obvious diffraction peak of rGO

in all composites, which is similar with the diffraction peak of pure TiO₂. This phenomena can be attributed to two aspects: on one hand, a compact membrane assembled by TiO₂ nanoparticles is attached to the surface of rGO, which leads to the decline of diffraction peak of rGO [37]; on the other hand, due to the lower content of rGO in the hybrid composites, the main characteristic reflection of carbon species is weak or probably shadowed by the (101) peak at 25.3° of anatase TiO₂ [38,39].

The morphologies of pure TiO₂ and rGTi-5 are characterized by SEM. The pure TiO₂ nanoparticles possess rough surface (Fig. 3a), while a smooth surface is presented in rGTi-5 (Fig. 3b), which may be attributed to the uniform coverage of TiO₂ nanoparticles on graphene sheet. Furthermore, compared to pure TiO₂, the background of rGTi-5 become blacker, suggesting the existence of carbon in GTi-5. Fig. 3c–f shows the TEM images of pure TiO₂ and of rGTi-5. Fig. 3c and d verifies that the typical constitution of pure TiO₂ is irregular spherical with mesostructure. Fig. 3e and f reveals that TiO₂ nanoparticles are well interspersed on the supporting flake-like wrinkled graphene sheet. Fig. 3g indicates the high crystallinity holds a plane spacing of 0.356 nm and 0.326 nm, corresponding to the spacing of (101) plane of anatase TiO₂ and spacing of (110) plane of rutile TiO₂. The SAED pattern of rGTi-5 (Fig. 3h) shows the clear ring diffraction patterns with the crystal lattice fringes. The rings from the inner to the outer structure correspond to the (101), (110), (004), (200) diffractions of the anatase phase and rutile phase [26], which are in agreement with the results of XRD. Fig. 4a–c depicts elemental mapping of Ti, O and C with distinct colors, respectively. It can be found that C elements are uniformly distributed in the rGTi-5. Besides, EDX spectrum (Fig. S1) further proves the presence of Ti, O and C elements in the rGTi-5. Therefore, it can be concluded that graphene has been successfully hybridized with TiO₂ nanoparticles.

3.1.2. Chemical bonding state

XPS spectra are used to ascertain the surface elemental composition and the valence state of rGTi-5. Fig. 5a presents that the fully scanned spectra of pure TiO₂ and rGTi-5. The elements of Ti, O and C appear in the pure TiO₂, where the small amount of C originated from the C pollution of XPS instrument. Also, the rGTi-5 contains elements of Ti, O and C, where the content of C is higher than that in pure TiO₂. It can be elucidated that the redundant of C is derived from graphene in the rGTi-5. Fig. 5b reveals that four peaks located at binding energies of 458.1 eV, 458.4 eV, 463.7 eV and 464.5 eV can be observed, which are assigned to Ti³⁺ 2p_{3/2}, Ti⁴⁺ 2p_{3/2}, Ti³⁺ 2p_{1/2}, and Ti⁴⁺ 2p_{1/2}, respectively [40]. Therefore, it can be seen that Ti³⁺ can be generated during the rGO-TiO₂ composites. It has been reported that the dope of Ti³⁺ could narrow the bandgap and extend the visible light absorption, which improves the visible light photocatalytic activity [41]. Therefore, Ti³⁺ (Ti³⁺/Ti⁴⁺ ratio) for all the catalyst are detected, which is shown in Table S1. It can be seen that with increase of graphene content, the quantities of Ti³⁺ increase but the quantities of Ti⁴⁺ decrease. The highest ratio of Ti³⁺ can reach 30.33% in the rGTi-7 sample. Therefore, it can be concluded that titania can be reduced to Ti³⁺. The increase of Ti³⁺ can enhance the adsorption range of light, which is in agreement with the result of UV–vis DRS (shown in the following section). Due to charge equilibrium, the presence of oxygen vacancies is always coupling with Ti³⁺ (Ti⁴⁺ + e[−] → Ti³⁺; O^{2−} − e[−] → O[−]) [42], which is also related to the enhancement of the photocatalytic properties. Therefore, XPS spectra of O1s is shown in Fig. 5c, which presents that the peaks at 529.9 eV, 530.5 eV and 531.6 eV corresponding to O-Ti⁴⁺, O-Ti³⁺ and surface hydroxyl groups (−OH), respectively. The result is consistent with the XPS result of Ti2p. According to the O1s and Ti2p fitting data, the O/Ti atomic ratio can be calculated through the element (or atom) in the sensitivity factors method [43]. The result is shown in Table S1. It can be seen that the O/Ti ratio of all the samples exceeds 2:1. However, the O/Ti ratio should be less than 2:1 based on the Ti2p fitting peak, where the titanium existed as Ti⁴⁺ and Ti³⁺.

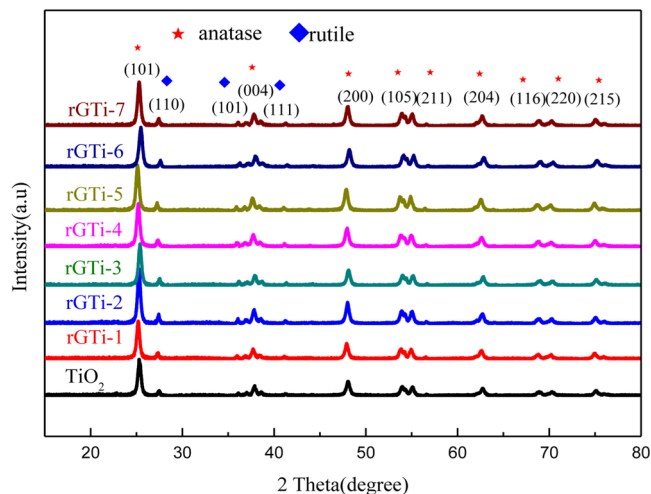


Fig. 2. XRD patterns of pure TiO₂ and rGO-TiO₂ samples.

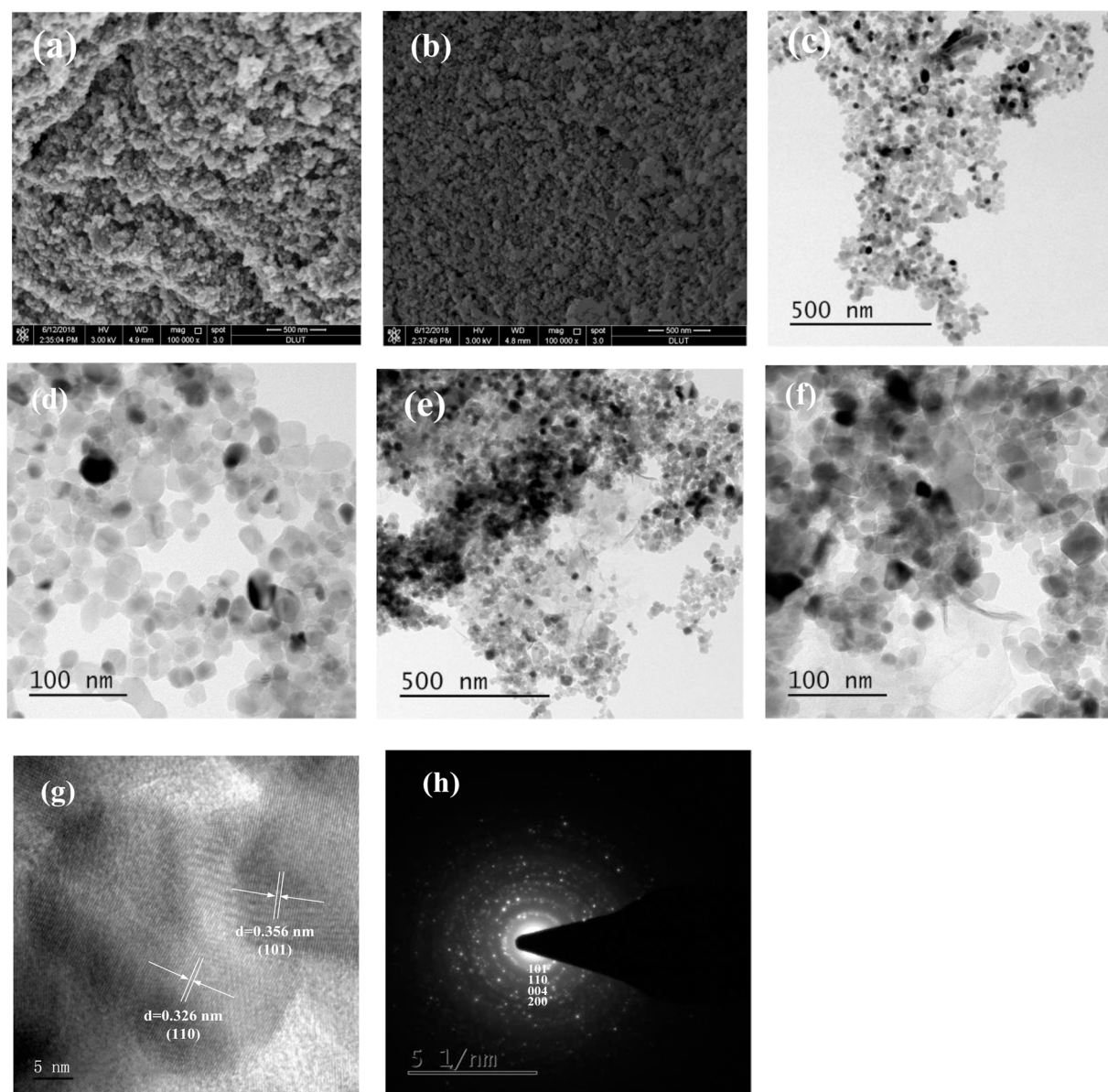


Fig. 3. SEM images of (a) pure TiO_2 , (b) rGTi-5; TEM images of (c, d) TiO_2 , (e, f) rGTi-5; (g) HRTEM image of rGTi-5; (h) SAED pattern of rGTi-5.

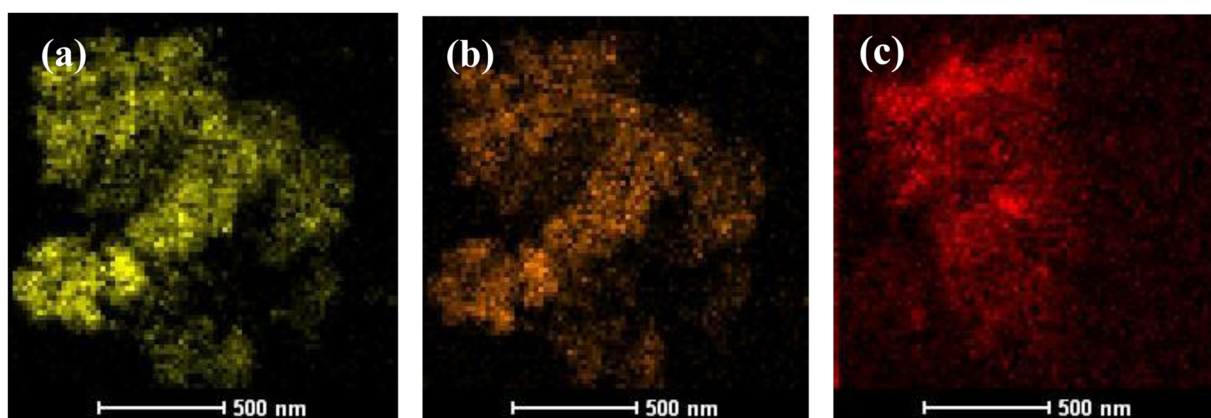


Fig. 4. EDS mapping images of the elements: (a) Ti, (b) O and (c) C on rGTi-5.

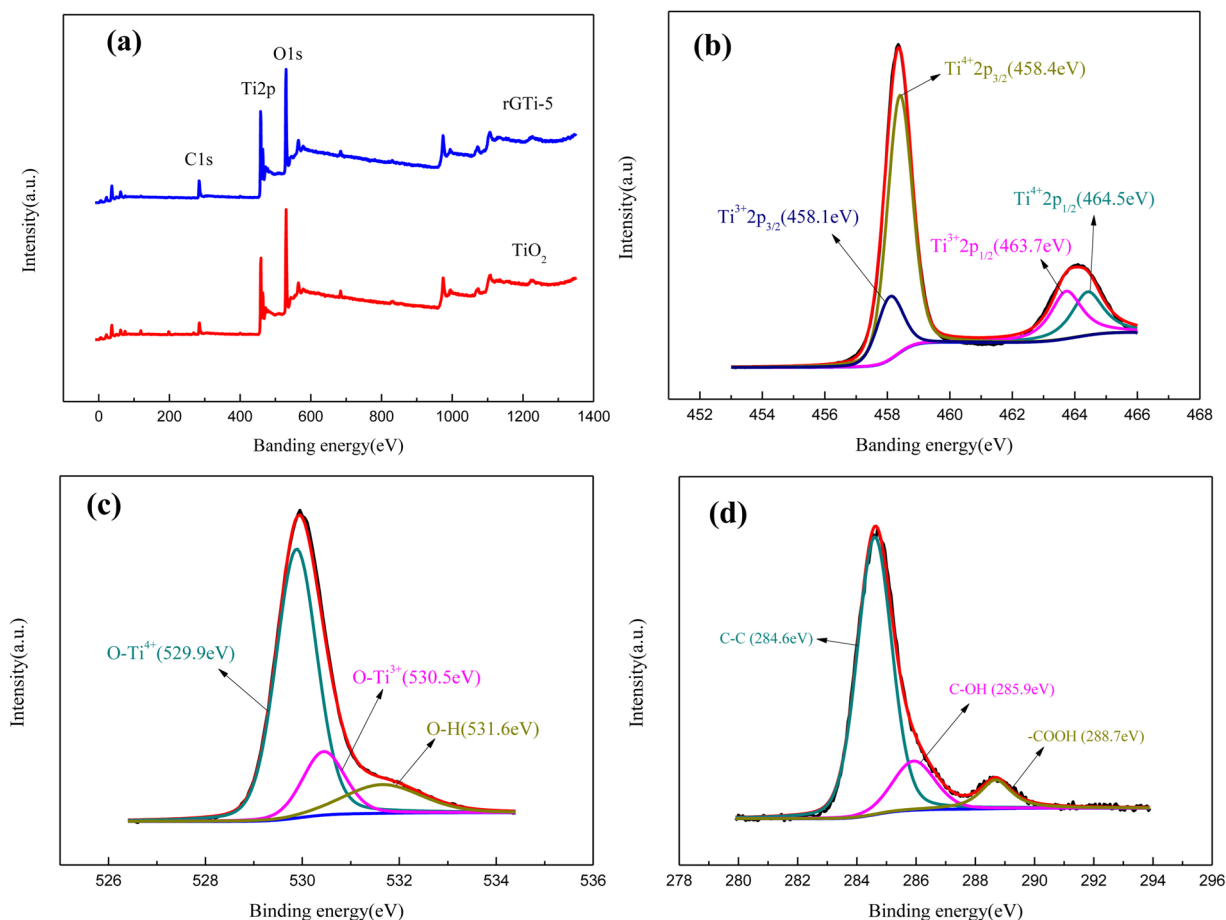


Fig. 5. XPS spectra for rGTi-5: (a) fully survey spectrum; (b) Ti2p; (c) O1s; (d) C1s.

Therefore, it can be verified that other active oxygen species such as hydroxyl groups of graphene exist in the catalyst surface besides the crystal lattice oxygen [44], which is in accordance with the above XPS spectra of O1s. The XPS spectra of C1s are detected and shown in Fig. 5d. It can be seen that three divided relevant fitting peaks with the binding energies of 284.6 eV, 285.9 eV and 288.7 eV are originated from the non-oxygenated ring C–C bonding, C–OH and –COOH, respectively [43]. Besides, C/Ti ratio for all catalysts is carried out by XPS and the results are shown in Table. 1. It can be seen that C/Ti ratio raises with the increase of graphene content. The improved C was mainly from the hybridization of graphene, which is in accordance with

the fitting results of the C1s.

Fig. 6a represents FT-IR spectra of pure TiO₂ and rGT-TiO₂ samples. The trend of FT-IR curve with different graphene content is similar. The broad and strong absorption peak at 400 to 700 cm^{−1} belongs to stretching vibration of Ti–O–Ti and Ti–O [45]. The Ti–O–C vibrations should appear at 535 cm^{−1} have not been detected clearly, which may be attributed to the lower content of graphene. The peak at 1400 cm^{−1} is ascribed to the characteristic absorption peak of Ti–O–Ti vibrations in TiO₂ [46]. The peak at 1630 cm^{−1} attached to aromatic C=C bonds is ascribed to the stretching and deformation vibrations of absorbed water [47]. The absorption peaks at 3000 cm^{−1} to 3500 cm^{−1}

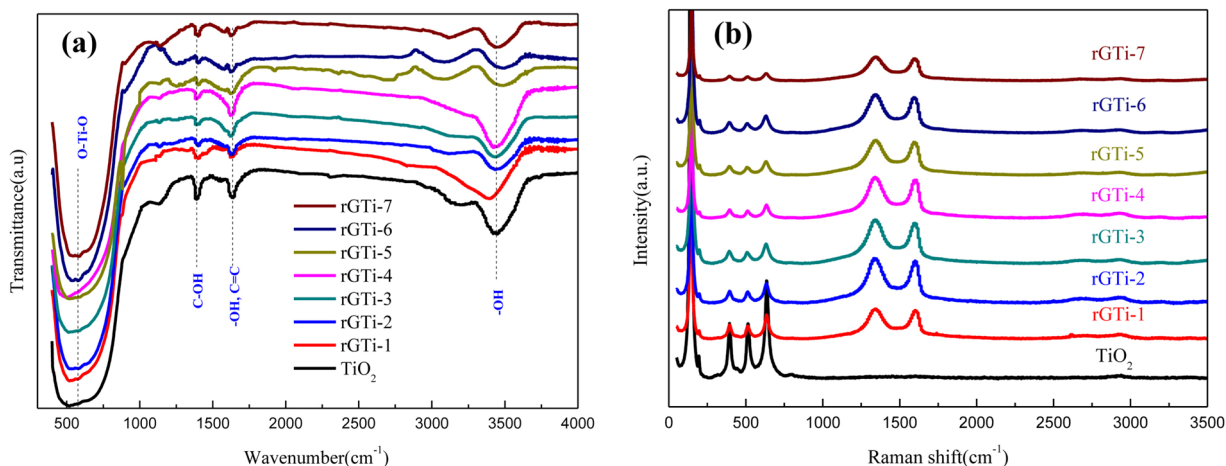


Fig. 6. FT-IR patterns (a) and Raman spectra (b) of pure TiO₂ and rGO-TiO₂ samples.

are assigned to the surface hydroxyl group or the absorbed water molecules [48].

Raman spectra of pure TiO_2 and rGO- TiO_2 samples with various graphene contents are shown in Fig. 6b. There are four Raman peaks located at $0\text{--}800\text{ cm}^{-1}$, which pertain to characteristic peaks of TiO_2 . The peaks at 144 cm^{-1} , 392 cm^{-1} , 516 cm^{-1} and 632 cm^{-1} are originated from anatase of TiO_2 , which are ascribed to the vibration of E_g , B_{1g} , A_{1g} and E_g , respectively [26]. Compared to the TiO_2 , there are two new peaks located at 1340 cm^{-1} and 1600 cm^{-1} appeared in the rGO- TiO_2 samples, which represent the symmetry A_{1g} and E_{2g} modes of sp^2 carbon atoms [49]. The characteristic peak at 1340 cm^{-1} is the D peak of graphene, which reflects the randomness of graphitic layers. The characteristic peak at 1600 cm^{-1} is the D peak of graphene, which states the symmetry and crystalline of graphene ($I_D/I_G = 1.15$) [37]. For the rGO- TiO_2 samples, the shift of the E_g mode at 144 cm^{-1} toward a higher wavenumber (shown in Fig. S2a), which is attributed to the structural defects such as oxygen vacancies and Ti^{3+} [50,51]. The Raman spectroscopy results are consistent with the XPS results. However, it is worth to note that there is no obvious characteristic peak related to the generated Ti^{3+} in the XRD patterns. It's because that the formed Ti^{3+} can introduced into the crystal lattice of TiO_2 nanosheets with exposed (001) facets during hydrothermal reaction [52]. Since (001) facet is the diffraction extinction surface, it is difficult to detected by XRD instrument based on the “extinction law” [53]. Therefore, the diffraction peaks of Ti^{3+} are not obvious in the XRD patterns. Furthermore, Fig. S2b shows that there is no obvious shift of graphene-related peaks with the increase of graphene content, which verifies the stable structure of graphene [26].

3.1.3. Optical property

Fig. 7a depicts the UV-vis DRS of TiO_2 and rGO- TiO_2 samples with various graphene contents. It is obvious noted that compare to the pure TiO_2 , the light absorption of the rGO- TiO_2 composite was improved. A red shift of $40\text{--}76\text{ nm}$ to longer wavelength regions appeared for the rGO- TiO_2 samples. The light absorption range can extend to 505 nm with the rGTi-7 sample. The result illustrates that the graphene significantly affects the optical properties of TiO_2 and then improves its photocatalytic activity. This may be attributed to the easier polarization of σ band generated by sp^2 hybrid carbon in graphene, which leads to a large Raman cross section. Besides, resonance of π state enhances when it is activated by visible light, which enhances the adsorption intensity of visible light. The conjugated big π bond generated by atomic bond of sp^2 hybrid carbon in graphene has an effective response to the visible light, which then raises the utilization of visible light [54]. In addition, as discussed in the above XPS analysis, the generated Ti^{3+} can enhance the adsorption range of light to the visible light. As to the high graphene content, the shift of the absorption band is difficult due to the enhanced

background adsorption on the incorporation of graphene into the matrix [37]. In addition, the band gaps (E_g) of pure TiO_2 and rGO- TiO_2 samples are estimated using a Tauc plot of the modified Kubelka-Munk (KM) function [55], which is shown in Fig. S3. It can be seen that the calculated band gap is about 2.84 eV for pure TiO_2 , which is about 2.62 eV , 2.56 eV , 2.54 eV , 2.52 eV , 2.49 eV , 2.46 eV and 2.45 eV for GTi-1, GTi-2, GTi-3, GTi-4, GTi-5, GTi-6 and GTi-7, respectively. The increase of graphene content leads to the decline of band gap, which is due to the improvement of Ti-C band formation in the composites and then form a new valence band [56].

The PL spectra are performed to explore recombination of electrons and holes. Generally, the lower PL intensity represents the lower recombination rate of photo-generated charge carriers. Fig. 7b depicts the PL spectra of TiO_2 and rGO- TiO_2 samples under the excitation wavelength at 300 nm . The emission bands are in the range of $450\text{--}490\text{ nm}$, which is assigned to luminescence from localized surface states due to recombination of photogenerated electron hole pairs [57]. Compared to the pure TiO_2 , the emission peak intensity of rGO- TiO_2 samples decreases, suggesting that the recombination rate of photo-generated charge carriers is lower. It can be also supposed that the rGO- TiO_2 samples have a high photonic efficiency and photocatalytic activity. Besides, it is also worth to note that with the increase of graphene content, the PL intensity first declines until 5 wt\% content and then enhances. This result can be assigned to that the excessive of graphene content makes the energy level of graphene as a recombination center of charge carriers [26]. Besides, PL spectra with an excitation wavelength at 435 nm are also carried out to justify this activity (shown in Fig. S4), which exhibits the similar result with that at excitation wavelength of 435 nm . Therefore, at 5 wt\% content, the graphene represents as an optimal charge carriers separation center.

3.1.4. Electrochemical property

Photocurrent density is used extensively for insight into the separation efficiency of the electrons and holes. Therefore, in the part, photocurrent densities for pure TiO_2 and rGO- TiO_2 samples are determined. As displayed in Fig. 8a, all the samples generate a photocurrent promptly, and the current densities of GTi- TiO_2 samples are higher than that of pure TiO_2 . The increase of graphene content first accelerates the current generation and then retards its generation. The highest current densities can be obtained at 5 wt\% content of rGO- TiO_2 samples, which is approximately four times as high as that of pure TiO_2 . Herein, it can be elucidated that the hybridization can promote the separation and transfer efficiency of photoinduced electrons and holes and thus induce the augment of the photocurrent density.

To further explore the charge transport capability, the EIS is recorded. In general, the smaller semicircle diameter suggests the lower resistance of electrode surface as well as the lower recombination rate

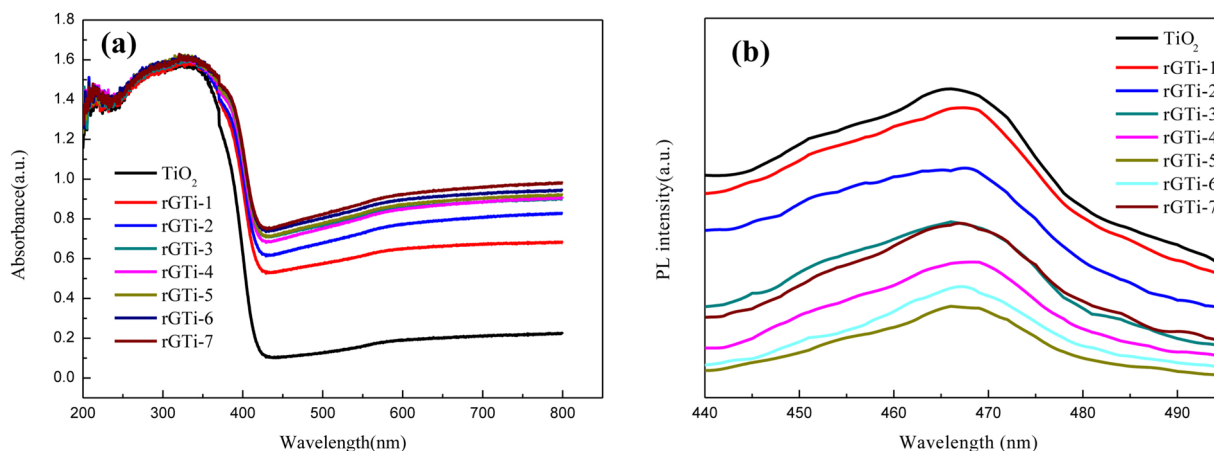


Fig. 7. UV-vis DRS (a) and PL spectrum (b) of pure TiO_2 and rGO- TiO_2 samples.

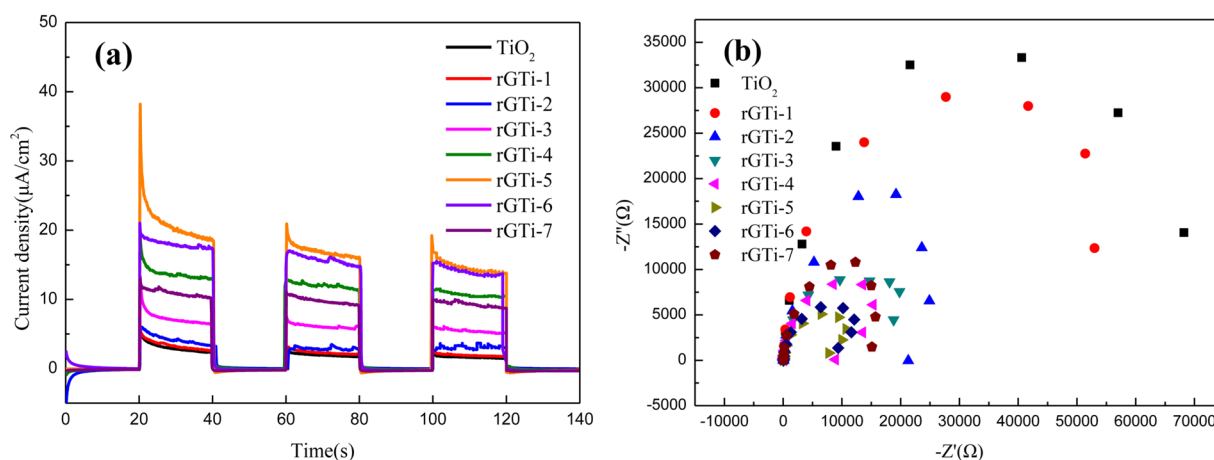


Fig. 8. Photocurrent densities (a) and EIS Nyquist plots (b) of pure TiO₂ and rGO-TiO₂ samples.

of photo-generated charge carriers [58]. As shown in Fig. 8b, the radii of the samples are as follows: TiO₂ > rGTi-1 > rGTi-2 > rGTi-3 > rGTi-7 > rGTi-4 > rGTi-6 > rGTi-5. It can be seen that the radii of rGO-TiO₂ samples are lower than that of pure TiO₂, which manifests the less resistance for charge transfer of rGO-TiO₂ samples. Furthermore, the GTi-5 sample has a smallest arc radius, suggesting the higher charge separation efficiency. These results are in agreement with that of PL spectra and the photocurrent.

3.2. Degradation performance with the prepared samples

Before degradation performance experiment, the emission spectrum is determined for figuring out the utilization of UV and visible light generated by PDP. It could be seen from Fig. S5 that the intensity of UV light (< 380 nm) is relatively weak. The relative higher intensity of spectrum mainly focuses on the range from 400 to 505 nm, which is dominated by the nitrogen lines from N₂ (C³π_u-B³π_g) [55]. According to optical property test, the absorption region of rGO-TiO₂ samples can range from 200 to 506 nm, which perfectly contains the higher intensity range of 400–505 nm.

The FLU degradation performance in PDP system with the prepared samples is evaluated and the result is shown in Fig. 9. It can be seen from Fig. 9a that the sole adsorption effect of GTi-5 sample is relatively little (6.6%) with 60 min adsorption time. When pure TiO₂ is added into PDP system, it is obviously noted that FLU removal efficiency enhances from 64.8% to 75.7% with 60 min treatment time. Compared to the pure TiO₂, the FLU removal efficiency can further enhance when rGO-TiO₂ samples are added. With the increase of graphene content, the FLU removal efficiency enhances first and then decreases. The FLU removal efficiency follows the order: TiO₂ < rGTi-1 < rGTi-2 < rGTi-3 < rGTi-7 < rGTi-4 < rGTi-6 < rGTi-5. Obviously, rGTi-5 exhibits the highest FLU removal efficiency (99.4%) with 60 min treatment time, which is 23.7% and 34.6% higher than that of PDP/TiO₂ system and sole PDP system, respectively. In addition, kinetic analysis of FLU degradation is carried out based on the first-order kinetic model (Fig. 9b). Analogously, the pure TiO₂ addition enhances the kinetic constant from 0.0167 min⁻¹ to 0.0216 min⁻¹ in the PDP system (Fig. 9c). The kinetic constant further raises with increasing the graphene ratio. When the graphene ratio is above 5%, the kinetic constant cannot improve any more, and actually decreases. Highest kinetic constant can reach 0.0767 min⁻¹ with the graphene ratio of 5%, and it is 3.5 and 4.6 times higher than that in sole PDP system (0.0167 min⁻¹) and PDP/TiO₂ system (0.0216 min⁻¹), respectively. Three aspects can be explained to this fact: on one hand, a high graphene content leads to the aggregation of graphene nano-sheets and TiO₂ nano-particles, resulting in the increase of the mass transfer resistance [27]. On the other hand, excess graphene content declines the light absorption capacity of

catalyst by reducing the contact area between TiO₂ and UV-vis light [54]. Moreover, the excessive of graphene content makes the energy level of graphene as a recombination center of charge carriers [39]. Fig. 9d represents the variation of UV spectra of FLU in PDP system with GTi-5 sample. The absorption peak of FLU at 326 nm gradually decreases with increasing the treatment time. After 60 min treatment time, absorption peak almost disappears, elucidating that most of the FLU can be eliminated by the combination process.

In order to illustrate the synergistic effect between PDP and rGO-TiO₂ samples, the synergistic factors are calculated according to the kinetic constant [60], which is shown in Table 1. It can be seen that synergistic factor of rGO-TiO₂ samples are higher than that of pure TiO₂, suggesting that the synergistic effect between PDP and rGO-TiO₂ samples is more clear. The highest synergistic factor reaches 4.27 with rGTi-5 addition, which is 2.43 times higher than that of pure TiO₂. All synergistic factors exceed 1 when rGO-TiO₂ samples added, indicating that a synergistic effect can be formed between PDP and rGO-TiO₂ samples. Furthermore, the energy efficiency under different reaction conditions is also given in Table 1. Compared to the sole pure TiO₂, the energy efficiency further enhances when rGO-TiO₂ samples are added, and the highest value can reach 10.86 mg/kJ with the rGTi-5. Therefore, it can be concluded that the rGO-TiO₂ samples promotes the energy utilization in the PDP system.

3.3. Reuse property

In order to explore the stability of the prepared sample, cycling degradation experiment is carried out. Fig. 10a displays the four times reusability of rGTi-5. It can be seen that the FLU removal efficiency declines with the increase of recycling times. After four times recycling, the FLU removal efficiency can maintain 86.3%, which declines about 13.0% compared to the first time cycling. Therefore, it can be seen that the prepared sample has a relative higher reusability although undergoing the discharge condition. In addition, the XRD pattern of rGTi-5 before and after use is tested, which is shown in Fig. 10b. It can be found that after four successive cycles, there is no obvious change between the fresh sample and used sample. Therefore, it can be concluded that the prepared sample has a higher reusability as well as stability.

3.4. Role of active species

In order to explore the contribution of various reactive species for FLU degradation in PDP system with or without rGTi-5, a series of scavenger test are performed. Isopropanol (IPA), sodium oxalate (SO) and p-benzoquinone (BQ) are adopted to investigate the role of ·OH, h⁺ and ·O₂⁻, respectively. It can be seen from Fig. 11a that all of IPA, SO and BQ retard FLU degradation performance from 64.8% to 51.3%,

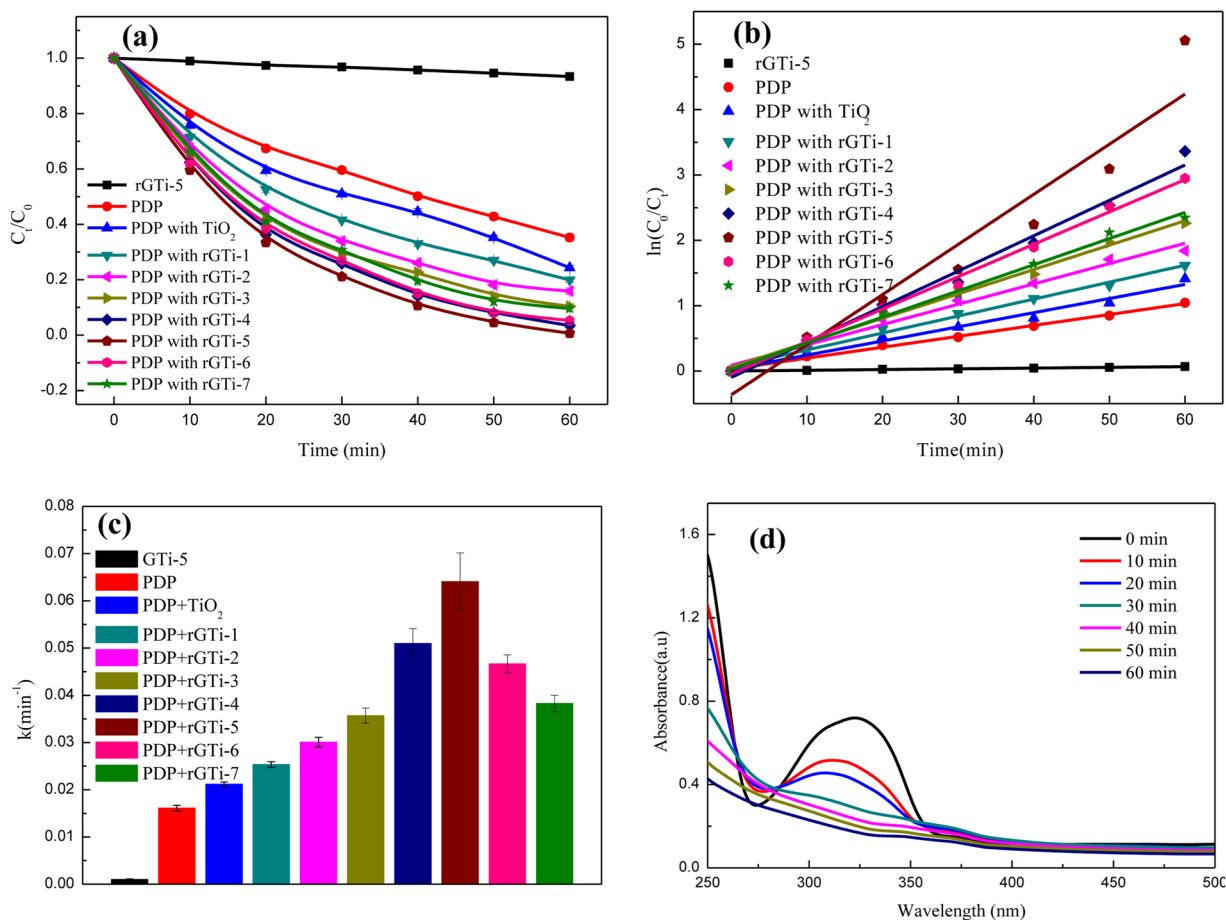


Fig. 9. (a) FLU degradation curves; (b) kinetic curves of FLU degradation; (c) kinetic rate for FLU degradation; (d) time-dependent UV-vis spectra of FLU solution by PDP with rGTi-5.

47.7% and 46.3%, respectively. It can be deduced that $\cdot\text{OH}$ and $\cdot\text{O}_2^-$ contribute to the FLU degradation. The decline of FLU removal efficiency when SO added is attributed to the change of solution conductivity and the change of discharge characteristic [20]. Fig. 11b suggests that three scavengers addition also makes for the decrease of FLU removal efficiency. For better comparison, the decline rate is calculated when scavengers are added with 60 min treatment time (Fig. 11c). It can be found that when rGTi-5 is added, the decline of FLU removal efficiency can reach 27.5%, 29.2% and 22.2% after IPA, SO and BQ addition, which are higher than that in the sole PDP system (13.5%, 17.4% and 18.5%, respectively). Therefore, it elucidates that $\cdot\text{OH}$, h^+ and $\cdot\text{O}_2^-$ play important role for photocatalytic degradation of FLU.

3.5. Generation of active species

In order to further make clear the photocatalytic mechanism, the production of O_3 , $\cdot\text{OH}$ and H_2O_2 in deionized water were detected after 60 min discharge time. Fig. 12a depicts the time profiles of O_3 production in PDP, PDP/ TiO_2 and PDP/rGTi-5 system. As time goes on, O_3 concentration first enhances and then decreases, and the highest value can reach 3.44 mg/L under 40 min treatment time. The decline of O_3

concentration after 40 min is mainly ascribed to its thermal decomposition. Moreover, compared to the sole PDP system, TiO_2 addition leads to the decline of O_3 concentration. It is assigned to that O_3 can be adsorbed on the surface of TiO_2 and then capture the conduction electrons, resulting in its decomposition and $\cdot\text{OH}$ generation (shown in Eqs. (2)–(4)) [61].



It is worth to note that O_3 concentration further declines when rGTi-5 is added in the system. The explanation to this fact lies in that the produced conduction electron can be transferred into the surface of graphene, which facilitates to the combination of O_3 and conduction electron. Meanwhile, the decomposition of O_3 was accelerated. In addition, it is interesting to note that O_3 concentration raise again after 40 min treatment time in PDP/ TiO_2 and PDP/rGTi-5 system, which is different from the trend in the sole PDP system. During experiment, we found that O_3 concentration in PDP/ TiO_2 and PDP/rGTi-5 system was

Table 1
Synergetic effect and energy efficiency under different reaction condition.

Condition	PDP	TiO_2	rGTi-1	rGTi-2	rGTi-3	rGTi-4	rGTi-5	rGTi-6	rGTi-7
Synergetic factor	1	1.27	1.52	1.80	2.14	3.08	4.27	2.76	2.21
Energy efficiency (mg/kJ)	7.08	8.27	8.76	9.20	9.79	10.55	10.86	10.36	9.88

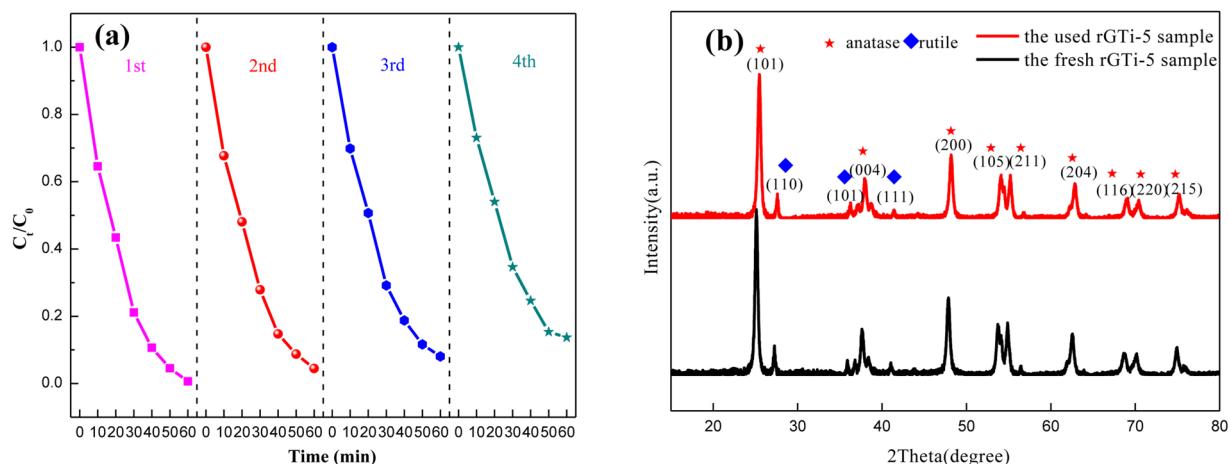


Fig. 10. (a) Cycling test of rGTi-5 sample; (b) XRD patterns of rGTi-5 before and after tests.

higher than that in sole PDP system after 60 min treatment time. It is suggested that the TiO_2 and rGTi-5 addition is also benefit for O_3 generation. It is because that the generated h^+ can react with $\text{O}^{\cdot -}$ and $\text{O}_2^{\cdot -}$, leading to O_3 generation (shown in Eqs. (5)–(9)) [62,63].



Fig. 12b portrays the variation of $\cdot\text{OH}$ concentration in PDP, PDP/ TiO_2 and PDP/rGTi-5 system. As expected, TiO_2 and rGTi-5 significantly enhance the $\cdot\text{OH}$ production. After 60 min treatment time, $\cdot\text{OH}$ concentration can reach 0.124 mmol/L, 0.160 mmol/L and 0.181 mmol/L in PDP, PDP/ TiO_2 and PDP/rGTi-5 system, respectively. During the pulsed discharge, $\cdot\text{OH}$ is mainly produced from the dissociation (Eq. (10)) and ionization (Eq. (11)) of water molecules [6,64,65].

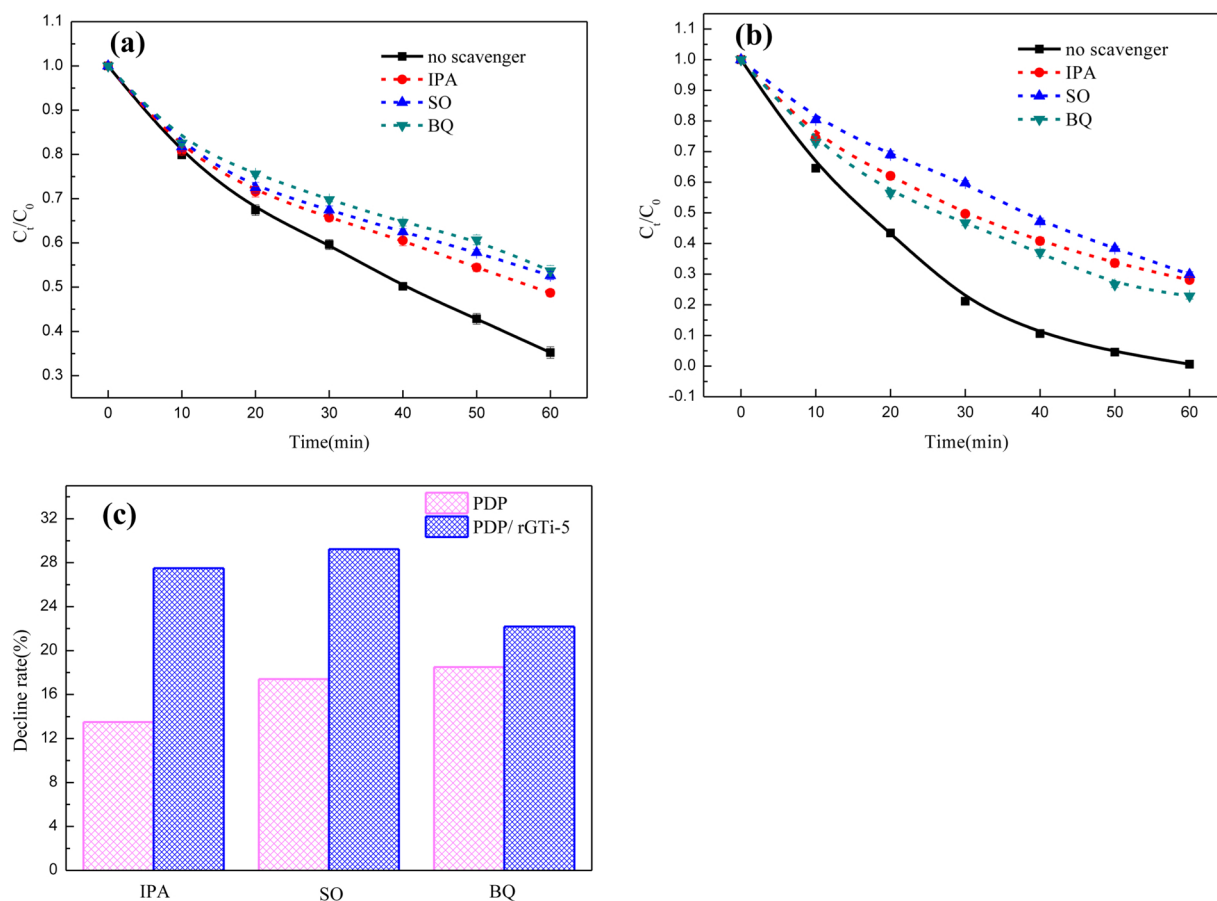
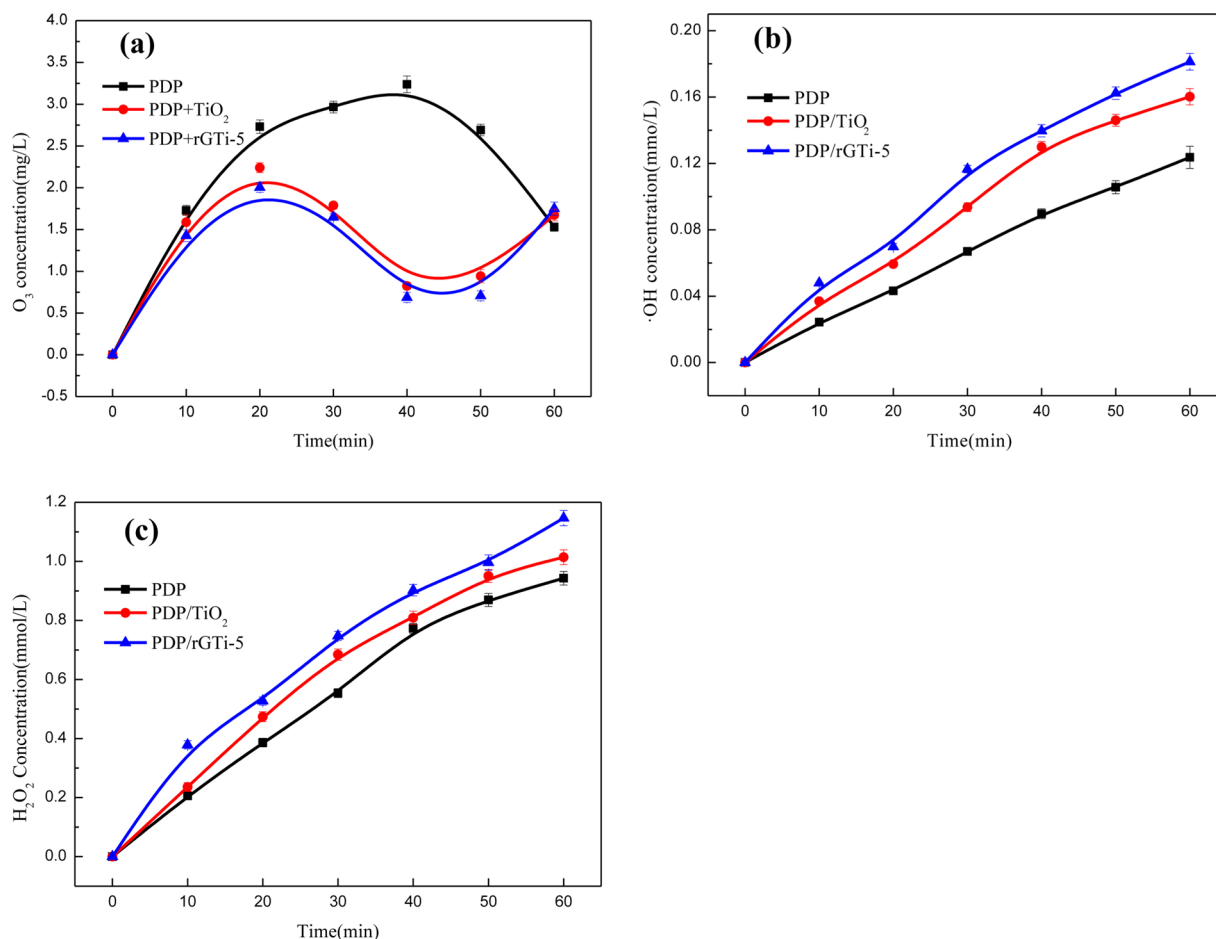


Fig. 11. Effects of reactive species scavengers on the FLU degradation (a) sole PDP system; (b) PDP with rGTi-5; (c) decline rate after addition of scavengers with 60 min treatment time.

Fig. 12. Generation of (a) O₃, (b) ·OH and (c) H₂O₂.

During photocatalysis process, on one hand, the generated h^+ can oxidize water molecules and leads to the generation of $\cdot\text{OH}$ (Eq. (13)). On the other hand, O_2 can react with conduction electron and results in the formation of $\cdot\text{O}_2^-$, which can be further transformed into $\cdot\text{OH}$ (Eqs. (6), (14) and (15)) [15,16,66]. Besides, as mentioned above, O_3 can also capture the conduction electron and induce the formation of $\cdot\text{OH}$. Therefore, it can be concluded that three major reactions accelerate the formation of $\cdot\text{OH}$, resulting in the enhancement of $\cdot\text{OH}$ concentration.



Due to the extremely short lifetime of $\cdot\text{OH}$, $\cdot\text{OH}$ hardly diffuse from the plasma zone into the surrounding water, which can quickly recombine with each other and form the H_2O_2 especially in the cases of underwater discharge (Eq. (16)) [6,67].



As shown in Fig. 12c, H_2O_2 variation trend is consistent with $\cdot\text{OH}$ variation trend, which further ascertains that the rGTi-5 is beneficial to $\cdot\text{OH}$ generation, which, as result, accelerates the decomposition of organic compounds.

3.6. Mineralization and 3DEEFM analysis

In order to evaluate the mineralization of FLU degradation, TOC removal in the sole PDP, PDP/TiO₂, and PDP/rGTi-5 system were explored. The TOC removal in PDP/rGTi-5 system can reach 35.8%, which is 8.6% and 4.8% higher than that in the sole PDP and PDP/TiO₂ system. Therefore, it can be illustrated that the rGTi-5 addition contributes to mineralization of FLU degradation. In addition, compared to the removal efficiency, the TOC removal is very lower, which suggests that there are many intermediates generated during FLU degradation, and it will be further explored in the following section.

3D EEFMs can be utilized for analyzing the fluorescent information of FLU in water due to the conjugate heterocyclic structures existed in the organic compounds molecules [68]. The fluorescence in different areas represents different components of molecules. In addition, the intensity of fluorescence suggests the concentration of organic compounds qualitatively. Thus, 3D EEFMs analysis was carried out to illustrate the variation of molecular structure and FLU concentration. It can be seen from Fig. 13a that the fluorescent peaks are located in the range of $\text{Ex/Em} = (220\text{--}250 \text{ nm})/(330\text{--}380 \text{ nm})$ and $\text{Ex/Em} = (250\text{--}400 \text{ nm})/(260\text{--}380 \text{ nm})$, which belong to the aromatic protein compounds (II) and soluble microbial by-product-like compounds (IV) respectively. With the time goes on, the intensity of two peak decrease, stating that the conjugate heterocyclic structures are broken and then leads to the generation of intermediates without conjugate heterocyclic structures (shown in Fig. 13b and c). Fig. 13d presents that two peaks disappeared after 60 min treatment, indicating that the PDP/rGTi-5 system can completely destroy conjugate heterocyclic structures of FLU. Therefore, it can be concluded that the PDP/

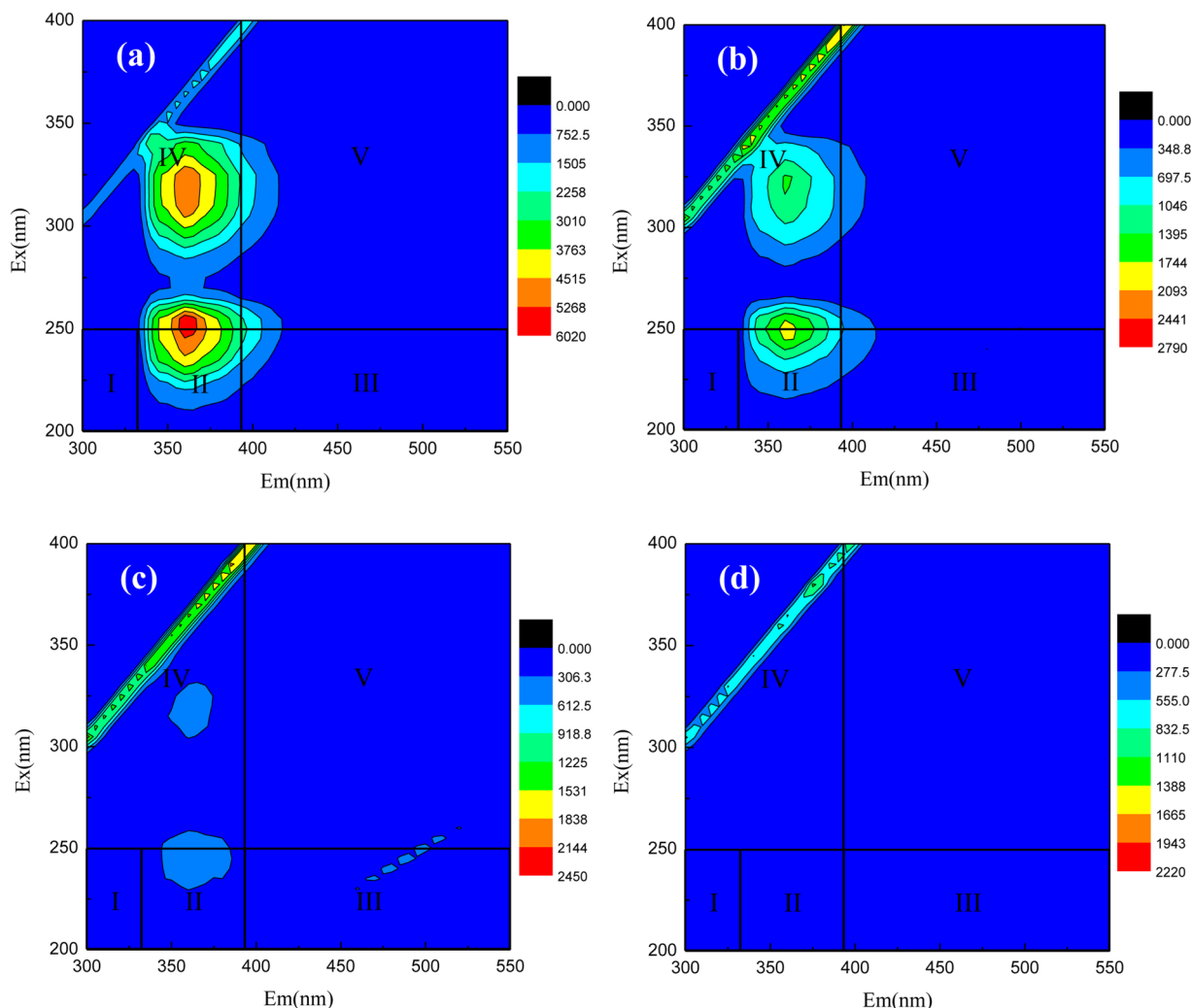


Fig. 13. 3D EEFMs of FLU solution after different PDP treatment time: (a) 0 min; (b) 20 min; (c) 40 min; (d) 60 min.

rGTi-5 system can effectively eliminate FLU in water.

3.7. Degradation intermediates and possible pathway

Based on the mineralization and 3DEEM analysis, it illustrates that there are many intermediates that can be generated during FLU degradation. Thus, the degradation intermediates are identified by LC–MS firstly, and the detailed information is exhibited in Table 2. It can be seen that there are eight intermediates that can be identified and the corresponding chromatograms are listed in Fig. S6.

According to the literatures and identified intermediates, there are two major pathways related to hydroxylation, decarbonylation and decarboxylation that can be proposed, which are shown in Fig. 14.

Pathway 1: the process is individually initiated by hydroxyl addition on the quinolone ring and makes for intermediate (5a) generation. Then, the olefinic double bond of the quinolone ring is attacked and leads to the opening of the ring. The reaction induces the formation of proposed (I) with two aldehyde groups, which is further transformed to proposed (II) by decarbonylation and decarboxylation [69]. The generated proposed (2) is subsequently oxidized by hydroxylation and leads to the formation of intermediate (2a). The carboxyl group of intermediate (2a) is ultimately substituted by a hydroxyl group and leads to the generation of intermediate (1a).

Pathway 2: the upper heterocyclic ring of FLU is firstly oxidized by hydroxylation, resulting in the formation of intermediate (5b). Next, two major ways can be put forward. Pathway 2a: the olefinic double

bond of the quinolone ring is broken down and forms two aldehyde groups, shown in intermediate (8). Then, decarbonylation or decarboxylation is occurred on intermediate (8) and forms proposed (III) or proposed (IV), which is further transformed to intermediate (2b) by a loss of carbonyl group or carboxyl group. This similar route was also reported in previous literature [70,71]. Finally, a further decarbonylation of intermediate (2b) results in the formation of intermediate (1b). Pathway 2b: the C–F bond of formed intermediate (5b) is cleaved and replaced by a hydroxyl group, which forms the intermediate (4). Then, the ring cleavage on the quinolone ring is occurred and produces intermediate (7) with two new aldehyde groups, which then lose a carbonyl group and generate the intermediate (6). Finally, the carboxyl group of intermediate (6) is substituted by a hydroxyl group and forms intermediate (3).

Subsequently, all the generated phenolic ring molecules are presumably further oxidized through ring-rupturing reactions and results in the formation of inorganic acid ions and organic acid ions, which are detected by IC. The formed inorganic acid ions included F^- and NO_3^- (shown in Fig. S7a), and similar results have been reported by Wen et al. [72]. The organic acid ions contain $HCOOH$, CH_3COOH and $HOCCOOH$ (shown in Fig. S7b and c), which are finally mineralized to CO_2 and H_2O .

3.8. Toxicity measure

While PDP with rGO–TiO₂ composites is effective for the

Table 2
FLU degradation intermediates detected by LC–MS.

No.	m/z	t_R	Molecular formula	Different with FLU	Chemical structure
1	210	18.57	$C_{11}H_{13}FNO_2$	– 3C1O	
2	238	10.97	$C_{12}H_{13}FNO_3$	– 2C	
3	252	2.93	$C_{12}H_{14}NO_5$	– 2C1F; + 1H ₂ O	
FLU	262	13.74	$C_{14}H_{13}FNO_3$	–	
4	276	9.19	$C_{14}H_{14}NO_5$	– 1F; + 1H ₂ O	
5	278	7.27	$C_{14}H_{13}FNO_4$	+ O	
6	280	2.61	$C_{13}H_{14}NO_6$	– 1C1F; + 1H ₃ O	
7	308	2.69	$C_{14}H_{14}NO_7$	– 1F; + 1H ₄ O	
8	310	3.08	$C_{14}H_{13}FNO_6$	+ 3O	

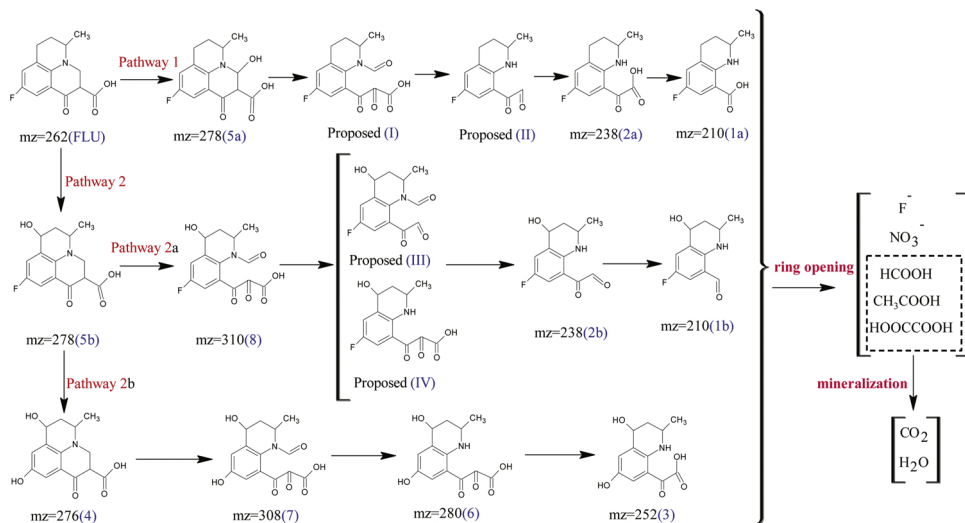


Fig. 14. Proposed pathway of FLU degradation in PDP/rGTi-5 system.

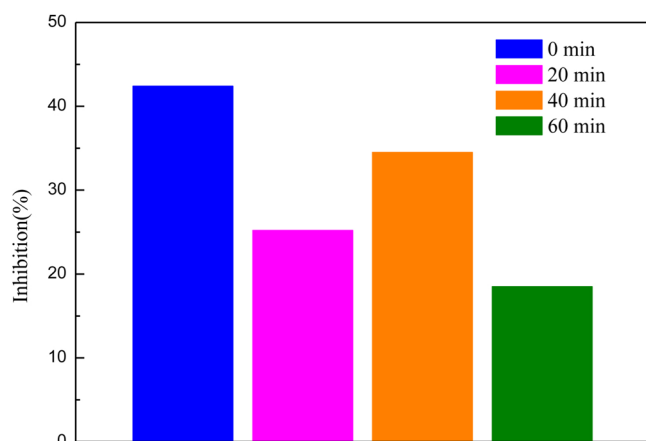


Fig. 15. Inhibition of FLU reaction solution with different reaction time.

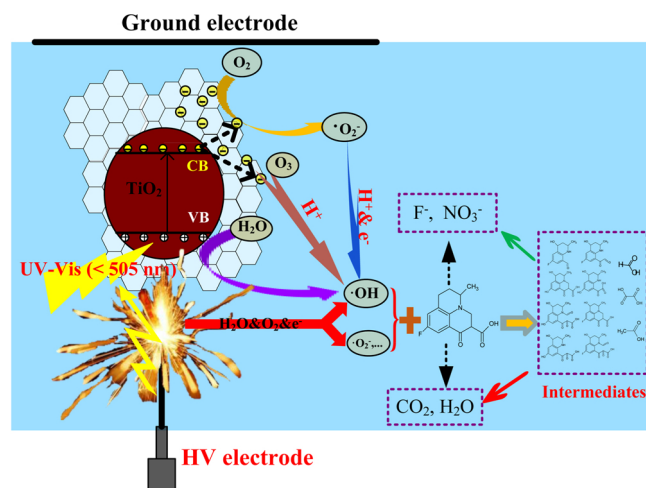


Fig. 16. The schematic illustration of FLU degradation mechanism by PDP with rGO-TiO₂ samples.

degradation of antibiotic FLU, another concern is the generation of oxidation by-products with certain enhanced or undesired toxic effects. Therefore, the toxicity evolution of the FLU solution treated by PDP with rGTi-5 was evaluated against *V. Fisheri* microorganisms [73].

Fig. 15 displays the toxic evolution of FLU reaction solutions after 0 min, 20 min, 40 min and 60 min of PDP/rG-5 treatment. It can be seen that the initial FLU solution exhibited 42.4% inhibition of bioluminescent activity, suggesting that the initial FLU solution exhibited significant adverse effects on the microorganisms. With 20 min treatment time, the inhibition of these treated solution for microorganisms was reduced. However, the inhibition was risen again with 40 min treatment time, which may be attributed to the generated several toxic products. After 60 min treatment, the inhibition fell to 18.5%, which is much lower than that in the initial FLU solution. It can be deduced that the toxicity in the treated FLU solution has reduced significantly at the end of the experiment. Therefore, it can be suggested that PDP with rGO-TiO₂ composites can be used as an effective but eco-friendly method to remove FLU in water.

3.9. Proposed degradation mechanism of FLU in PDP/rGO-TiO₂ system

Based on the above various characterization analysis and mechanistic exploration, the schematic illustration of FLU degradation mechanism by PDP with rGO-TiO₂ samples is summarized in Fig. 16. The generated UV-vis light (< 505 nm) by PDP induces the TiO₂ on the surface of graphene sheet and leads to the separation of electron-hole

pairs. The generated h^+ can react with H₂O or OH[−] to produce the ·OH. The generated conduction electrons can transfer into the graphene, and then captured by both O₂ in the liquid and O₃ generated by PDP, which further generates ·OH. The existence of graphene broadens the light adsorption range, accelerates the electron transfer and provides more active site, resulting in more ·OH generation. The generated ·OH by photocatalysis together with the ·OH, ·O₂[−], etc. generated by PDP joint react with FLU molecules. The process induces the generation of intermediates, which are eventually oxidized to F[−], NO₃[−], CO₂ and H₂O.

4. Conclusion

In the study, we prepared rGO-TiO₂ hybrid nanocomposites for synergistic degradation of FLU degradation PDP system. Various characteristic methods demonstrate that rGO-TiO₂ samples have been successfully prepared by a hydrothermal method, and exhibit the higher light adsorption range and faster separation of electron-hole pairs. The degradation performance experiment shows that the rGTi-5 exhibits the highest catalytic performance with 99.4% removal efficiency in PDP system, which is higher than 64.8% in the sole PDP system. The reuse test suggests that the prepared rGO-TiO₂ samples have a higher reusability as well as stability. The generated ·OH, h^+ and ·O₂[−] make contribution to the photocatalytic degradation of FLU. The enhancement of FLU removal efficiency is ascribed to the increase of ·OH driven from h^+ oxidation and conduction electron captured by O₂ and O₃. 3DEEM demonstrate that the conjugate heterocyclic structures of FLU can be destroyed by the PDP/rGO-TiO₂ process. The LC-MS and IC determination illustrate that eight phenolic ring molecules and three small molecules can be produced, which can be further oxidized to F[−], NO₃[−], CO₂ and H₂O. After PDP/rGO-TiO₂ treatment, the toxicity in the treated FLU solution significantly reduced. These processes would become a promising technology of non-thermal plasma coupled with graphene-based nanocomposites for energy promotion and environmental remediation.

Acknowledgements

We greatly appreciate financial support from National Natural Science Foundation of China (No. 21876070).

Appendix A. Supplementary data

Supplementary data associated with this article can be found, in the online version, at <https://doi.org/10.1016/j.apcatb.2019.01.052>.

References

- [1] K. Kümmerer, Antibiotics in the aquatic environment—a review—part I, *Chemosphere* 75 (2009) 417–434.
- [2] F.L. Wang, Y. Feng, P. Chen, Y.F. Wang, Y.H. Su, Q.X. Zhang, Y.Q. Zeng, Z.J. Xie, H.J. Liu, Y. Liu, W.Y. Lv, G.G. Liu, Photocatalytic degradation of fluoroquinolone antibiotics using ordered mesoporous g-C₃N₄, under simulated sunlight irradiation: kinetics, mechanism, and antibacterial activity elimination, *Appl. Catal. B: Environ.* 227 (2018) 114–122.
- [3] M. Čvančarová, M. Moeder, A. Filipová, T. Reemtsma, T. Cajthaml, Biotransformation of the antibiotic agent flumequine by ligninolytic fungi and residual antibacterial activity of the transformation mixtures, *Environ. Sci. Technol.* 47 (2013) 14128–14136.
- [4] G.L. Chen, M. Li, X. Liu, Fluoroquinolone antibacterial agent contaminants in soil/groundwater: a literature review of sources, fate, and occurrence, *Water Air Soil Pollut.* 226 (2015) 418.
- [5] P. Sukul, M. Spittler, Fluoroquinolone antibiotics in the environment, *Rev. Environ. Contam. Toxicol.* 191 (2007) 131–162.
- [6] B. Jiang, J.T. Zheng, S. Qiu, M.B. Wu, Q.H. Zhang, Z.F. Yan, Q.Z. Xue, Review on electrical discharge plasma technology for wastewater remediation, *Chem. Eng. J.* 236 (2014) 348–368.
- [7] J.V. Durme, J. Dewulf, C. Leys, V.H. Langenhove, Combining non-thermal plasma with heterogeneous catalysis in waste gas treatment: a review, *Appl. Catal. B: Environ.* 78 (2008) 324–333.
- [8] H. Zhang, D.Y. Ma, R.L. Qiu, Y.T. Tang, C.M. Du, Non-thermal plasma technology

- for organic contaminated soil remediation: a review, *Chem. Eng. J.* 313 (2017) 157–170.
- [9] H.J. Wang, J. Li, X. Quan, Decoloration of azo dye by a multi-needle-to-plate high-voltage pulsed corona discharge system in water, *J. Electrostat.* 64 (2006) 416–421.
- [10] J. Li, M. Sato, T. Ohshima, Degradation of phenol in water using a gas–liquid phase pulsed discharge plasma reactor, *Thin Solid Films* 515 (2007) 4283–4288.
- [11] O. Khalifeh, A. Mosallanejad, H. Taghvaei, M.R. Rahimpour, A. Shariati, Decomposition of methane to hydrogen using nanosecond pulsed plasma reactor with different active volumes, voltages and frequencies, *Appl. Energ.* 169 (2016) 585–596.
- [12] W.J. Bian, X.L. Ying, J.W. Shi, Enhanced degradation of p-chlorophenol in a novel pulsed high voltage discharge reactor, *J. Hazard. Mater.* 162 (2009) 906–912.
- [13] J. Pawlat, K. Hensel, S. Ihara, Decomposition of humic acid and methylene blue by electric discharge in foam, *Acta Phys. Slovaca* 55 (2005) 479–485.
- [14] H.J. Wang, J. Li, X. Quan, Y. Wu, Enhanced generation of oxidative species and phenol degradation in a discharge plasma system coupled with TiO₂ photocatalysis, *Appl. Catal. B: Environ.* 83 (2008) 72–77.
- [15] H.J. Wang, J. Li, X. Quan, Y. Wu, G.F. Li, F.Z. Wang, Formation of hydrogen peroxide and degradation of phenol in synergistic system of pulsed corona discharge combined with TiO₂ photocatalysis, *J. Hazard. Mater.* 141 (2007) 336–343.
- [16] X.L. Hao, M.H. Zhou, Y. Zhang, L.C. Lei, Enhanced degradation of organic pollutant 4-chlorophenol in water by non-thermal plasma process with TiO₂, *Plasma Chem. Plasma Process.* 26 (2006) 455–468.
- [17] J. Li, Z.G. Zhou, H.J. Wang, G.F. Li, Y. Li, Research on decoloration of dye wastewater by combination of pulsed discharge plasma and TiO₂ nanoparticles, *Desalination* 212 (2007) 123–128.
- [18] Y. Zhang, Q. Xin, Y.Q. Cong, B.Q. Jiang, Application of TiO₂ nanotubes with pulsed plasma for phenol degradation, *Chem. Eng. J.* 215 (2013) 261–268.
- [19] Y. Zhang, J.N. Lu, X.P. Wang, Q. Xin, Y.Q. Cong, Q. Wang, C.J. Li, Phenol degradation by TiO₂ photocatalysts combined with different pulsed discharge systems, *J. Colloid Interface Sci.* 409 (2013) 104–111.
- [20] B. Sun, M. Sato, J.S. Clements, Optical study of active species produced by a pulsed streamer corona discharge in water, *J. Electrostat.* 39 (1997) 189–202.
- [21] J. Dunn, Pulsed-light treatment of food and packaging, *Food Technol.* 49 (1995) 95–98.
- [22] K.S. Novoselov, A.K. Geim, S.V. Morozov, D. Jiang, Y. Zhang, S.V. Dubonos, I.V. Grigorieva, A.A. Firsov, Electric field effect in atomically thin carbon films, *Science* 306 (2004) 666–669.
- [23] K.I. Bolotin, K.J. Sikes, Z. Jiang, M. Klima, G. Fudenberg, J. Hone, P. Kim, H.L. Stormer, Ultrahigh electron mobility in suspended graphene, *Solid State Commun.* 146 (2008) 351–355.
- [24] X. Du, I. Skachko, A. Barker, E.Y. Andrei, Approaching ballistic transport in suspended graphene, *Nat. Nanotechnol.* 3 (2008) 491.
- [25] R.R. Nair, P. Blake, A.N. Grigorenko, K.S. Novoselov, T.J. Booth, T. Stauber, N.M. Peres, A.K. Geim, Fine structure constant defines visual transparency of graphene, *Science* 320 (2008) 1308.
- [26] K. Li, J. Xiong, T. Chen, L.S. Yan, Y.H. Dai, D.Y. Song, Y. Lv, Z.X. Zeng, Preparation of graphene/TiO₂ composites by nonionic surfactant strategy and their simulated sunlight and visible light photocatalytic activity towards representative aqueous POPs degradation, *J. Hazard. Mater.* 250 (2013) 19–28.
- [27] G.H. Moon, D.H. Kim, H.I. Kim, A.D. Bokare, W. Choi, Platinum-like behavior of reduced graphene oxide as a cocatalyst on TiO₂ for the efficient photocatalytic oxidation of arsenite, *Environ. Sci. Technol. Lett.* 1 (2014) 185–190.
- [28] R.C. Pawar, D. Cho, C.S. Lee, Fabrication of nanocomposite photocatalysts from zinc oxide nanostructures and reduced graphene oxide, *Curr. Appl. Phys.* 13 (2013) S50–S57.
- [29] E. Diamantopoulou, G.E. Sakellis, S. Romanos, N. Gardelis, N. Ioannidis, P. Boukos, V. Falaras, Likodimos, Titania photonic crystal photocatalysts functionalized by graphene oxide nanocolloids, *Appl. Catal. B: Environ.* 240 (2019) 277–290.
- [30] L.M. Pastrana-Martínez, S. Morales-Torres, V. Likodimos, P. Falaras, J.L. Figueiredo, J.L. Faria, A.M. Silva, Role of oxygen functionalities on the synthesis of photocatalytically active graphene-TiO₂ composites, *Appl. Catal. B: Environ.* 158 (2014) 329–340.
- [31] E. Zong, D. Wei, H.Q. Wan, S.R. Zheng, Z.Y. Xu, D.Q. Zhu, Adsorptive removal of phosphate ions from aqueous solution using zirconia-functionalized graphite oxide, *Chem. Eng. J.* 221 (2013) 193–203.
- [32] O. Akhavan, M. Choobtashani, E. Ghaderi, Protein degradation and RNA efflux of viruses photocatalyzed by graphene–tungsten oxide composite under visible light irradiation, *J. Phys. Chem. C* 116 (2012) 9653–9659.
- [33] L.B. Jiang, X.Z. Yuan, G.M. Zeng, J. Liang, Z.B. Wu, H. Wang, Construction of all-solid-state Z-scheme photocatalyst based on graphite carbon nitride and its enhancement to catalytic activity, *Environ. Sci. Nano* 5 (2018) 599–615.
- [34] N. Jiang, L.J. Guo, Y. Zhang, K.F. Shang, N. Lu, J. Li, Y. Wu, Reactive species distribution characteristics and toluene destruction in the three-electrode DBD reactor energized by different pulsed modes, *Chem. Eng. J.* 350 (2018) 12–19.
- [35] L. Diez, M.H. Livertoux, A.A. Stark, M. Ellmanrousseau, W.P. Leroy, High-performance liquid chromatographic assay of hydroxyl free radical using salicylic acid hydroxylation during in vitro experiments involving thiols, *J. Chromatogr. B* 763 (2001) 185–193.
- [36] H.J. Wang, H. Guo, Q.S. Wu, G.S. Zhou, C.W. Yi, Effect of activated carbon addition on H₂O₂ formation and dye decoloration in a pulsed discharge plasma system, *Vacuum* 128 (2016) 99–105.
- [37] M.H. Zhu, X. Li, W.W. Liu, Y. Cui, An investigation on the photoelectrochemical properties of dye-sensitized solar cells based on graphene–TiO₂ composite photoanodes, *J. Power Sources* 262 (2014) 349–355.
- [38] N.R. Khalid, E. Ahmed, Z. Hong, L. Sana, M. Ahmed, Enhanced photocatalytic activity of graphene–TiO₂ composite under visible light irradiation, *Curr. Appl. Phys.* 13 (2013) 659–663.
- [39] Y. Zhang, Z.R. Tang, X. Fu, Y.J. Xu, TiO₂-graphene nanocomposites for gas-phase photocatalytic degradation of volatile aromatic pollutant: is TiO₂-graphene truly different from other TiO₂-carbon composite materials? *ACS Nano* 4 (2010) 7303–7314.
- [40] X. Yu, X.L. Fan, L. An, G.B. Liu, Z.H. Li, J.W. Liu, P.A. Hu, Mesocrystalline Ti³⁺-TiO₂ hybridized gC₃N₄ for efficient visible-light photocatalysis, *Carbon* 128 (2018) 21–30.
- [41] D. Qi, L. Lu, Z. Xi, L. Wang, J. Zhang, Enhanced photocatalytic performance of TiO₂ based on synergistic effect of Ti³⁺ self-doping and slow light effect, *Appl. Catal. B: Environ.* 160 (2014) 621–628.
- [42] J. Tang, Y. Liu, Y. Hu, G. Lv, C. Yang, G. Yang, Carbothermal reduction induced Ti³⁺ self-doped TiO₂/GQD nanohybrids for high performance visible light photocatalysis, *Chem.: Eur. J.* 24 (2018) 4390–4398.
- [43] S. Cao, T. Liu, Y. Tsang, C. Chen, Role of hydroxylation modification on the structure and property of reduced graphene oxide/TiO₂ hybrids, *Appl. Surf. Sci.* 382 (2016) 225–238.
- [44] C.H. Kim, B.H. Kim, K.S. Yang, TiO₂ nanoparticles loaded on graphene/carbon composite nanofibers by electrospinning for increased photocatalysis, *Carbon* 50 (2012) 2472–2481.
- [45] G.Z. Liao, D.Y. Zhu, J.X. Zheng, J. Yin, B.Y. Lan, L.S. Li, Efficient mineralization of bisphenol A by photocatalytic ozonation with TiO₂-graphene hybrid, *J. Taiwan Inst. Chem. Eng.* 67 (2016) 300–305.
- [46] C.H. Huang, H.L. Bai, Y.L. Huang, S.L. Liu, S.I. Yen, Y.S. Tseng, Synthesis of neutral SiO₂/TiO₂ hydrosol and its application as antireflective self-cleaning thin film, *Int. J. Photoenergy* 2012 (2012) 620764.
- [47] H. Ding, S. Zhang, J.T. Chen, X.P. Hu, Z.F. Du, Y.X. Qiu, D.L. Zhao, Reduction of graphene oxide at room temperature with vitamin C for RGO–TiO₂ photoanodes in dye-sensitized solar cell, *Thin Solid Films* 584 (2015) 29–36.
- [48] N. Boonprakob, N. Wetchakun, S. Phanichphant, D. Waxler, P. Sherrell, A. Nattestad, J. Chen, B. Inceesungvor, Enhanced visible-light photocatalytic activity of g-C₃N₄/TiO₂ films, *J. Colloid Interface Sci.* 417 (2014) 402–409.
- [49] J.F. Shen, Y.Z. Hu, M. Shi, N. Li, H.W. Ma, M.X. Ye, One step synthesis of graphene oxide–magnetic nanoparticle composite, *J. Phys. Chem. C* 114 (2010) 1498–1503.
- [50] C. Wang, D. Meng, J. Sun, J. Memon, Y. Huang, J. Geng, Graphene wrapped TiO₂ based catalysts with enhanced photocatalytic activity, *Adv. Mater. Interfaces* 1 (2014) 1300150.
- [51] G. Rajender, J. Kumar, P.K. Giri, Interfacial charge transfer in oxygen deficient TiO₂-graphene quantum dot hybrid and its influence on the enhanced visible light photocatalysis, *Appl. Catal. B: Environ.* 224 (2018) 960–972.
- [52] J. Cai, K. Lv, J. Sun, K. Deng, Ti powder-assisted synthesis of Ti³⁺ self-doped TiO₂ nanosheets with enhanced visible-light photoactivity, *RSC Adv.* 4 (2014) 19588–19593.
- [53] H. Ming, P. Kumar, W. Yang, Y. Fu, J. Ming, W.J. Kwak, Green strategy to single crystalline anatase TiO₂ nanosheets with dominant (001) facets and its lithiation study toward sustainable cobalt-free lithium ion full battery, *ACS Sustain. Chem. Eng.* 3 (2015) 3086–3095.
- [54] X. Hu, C. Hu, Preparation and visible-light photocatalytic activity of Ag₃VO₄ powders, *J. Solid State Chem.* 180 (2007) 725–732.
- [55] L.J. Duan, N. Jiang, N. Lu, K.F. Shang, J. Li, Y. Wu, Synergetic effect of TiO₂ and Fe³⁺ as co-catalysts for enhanced phenol degradation in pulsed discharge system, *Appl. Catal. B: Environ.* 221 (2018) 521–529.
- [56] S. Sakthivel, K. Horst, Daylight photocatalysis by carbon-modified titanium dioxide, *Angew. Chem. Int. Ed.* 42 (2003) 4908–4911.
- [57] X. Huang, L.Y. Wang, J.Z. Zhou, N.Y. Gao, Photocatalytic decomposition of bromate ion by the UV/P25-Graphene processes, *Water Res.* 57 (2014) 1–7.
- [58] X.J. Wen, C.G. Niu, L. Zhang, C. Liang, G.M. Zeng, A novel Ag₂O/CeO₂ heterojunction photocatalysts for photocatalytic degradation of enrofloxacin: possible degradation pathways, mineralization activity and an in depth mechanism insight, *Appl. Catal. B: Environ.* 221 (2018) 701–704.
- [60] K.F. Shang, X.J. Wang, J. Li, H. Wang, N. Lu, N. Jiang, Y. Wu, Synergetic degradation of acid orange 7 (AO7) dye by DBD Plasma and persulfate, *Chem. Eng. J.* 311 (2017) 378–384.
- [61] J.F. Gomes, I. Leal, K. Bednarczyk, M. Gmurek, M. Stelmachowski, M. Diak, Q.M. Emília, R. Costa, R.M. Quinta-Ferreira, R.C. Martins, Photocatalytic ozonation using doped TiO₂ catalysts for the removal of parabens in water, *Sci. Total Environ.* 609 (2017) 329–340.
- [62] M. Simek, C. Martin, Efficiency of ozone production by pulsed positive corona discharge in synthetic air, *J. Phys. D: Appl. Phys.* 35 (2002) 1171.
- [63] M.R. Ghezfar, F. Abdelmalek, M. Belhadj, N. Benderdouche, A. Addou, Gliding arc plasma assisted photocatalytic degradation of anthraquinonic acid green 25 in solution with TiO₂, *Appl. Catal. B: Environ.* 72 (2007) 304–313.
- [64] A.A. Joshi, B.R. Locke, P. Arce, W.C. Finney, Formation of hydroxyl radicals, hydrogen peroxide and aqueous electrons by pulsed streamer corona discharge in aqueous solution, *J. Hazard. Mater.* 41 (1995) 3–30.
- [65] R.P. Joshi, S.M. Thagard, Streamer-like electrical discharges in water: Part II. Environmental applications, *Plasma Chem. Plasma Process.* 33 (2013) 17–49.
- [66] U.G. Akpan, B.H. Hameed, Parameters affecting the photocatalytic degradation of dyes using TiO₂-based photocatalysts: a review, *J. Hazard. Mater.* 170 (2009) 520–529.
- [67] R. Roots, S. Okada, Estimation of life times and diffusion distances of radicals involved in X-ray-induced DNA strand breaks or killing of mammalian cells, *Radiat. Res.* 64 (1975) 306–320.
- [68] W. Chen, P. Westerhoff, J.A. Leenheer, K. Booksh, Fluorescence excitation-emission matrix regional integration to quantify spectra for dissolved organic matter,

- Environ. Sci. Technol. 37 (2003) 5701–5710.
- [69] M.B. Feng, X.H. Wang, J. Chen, R.G. Qu, Y.X. Sun, L. Cizmas, Z.Y. Wang, V.K. Sharma, Degradation of fluoroquinolone antibiotics by ferrate (VI): effects of water constituents and oxidized products, *Water Res.* 103 (2016) 48–57.
- [70] W. Lou, A. Kane, D. Wolbert, S. Rtimi, A.A. Assadi, Study of a photocatalytic process for removal of antibiotics from wastewater in a falling film photoreactor: scavenger study and process intensification feasibility, *Chem. Eng. Process. Process Int.* 122 (2017) 213–221.
- [71] M.B. Feng, L.Q. Yan, X.L. Zhang, P. Sun, S.G. Yang, L.S. Wang, Z.Y. Wang, Fast removal of the antibiotic flumequine from aqueous solution by ozonation: influencing factors, reaction pathways, and toxicity evaluation, *Sci. Total Environ.* 541 (2016) 167–175.
- [72] X.J. Wen, C.G. Niu, L. Zhang, C. Liang, H. Guo, G.M. Zeng, Photocatalytic degradation of ciprofloxacin by a novel Z-scheme $\text{CeO}_2\text{-Ag/AgBr}$ photocatalyst: influencing factors, possible degradation pathways, and mechanism insight, *J. Catal.* 358 (2018) 141–154.
- [73] A.A. Bulich, D.L. Isenberg, Use of the luminescent bacterial system for the rapid assessment of aquatic toxicity, *ISA Trans.* 20 (2012) 29–33.

Further reading

- [59] N. Yang, J. Zhai, D. Wang, Y. Chen, L. Jiang, Two-dimensional graphene bridges enhanced photoinduced charge transport in dye-sensitized solar cells, *ACS Nano* 4 (2010) 887–894.